

Title	Development of a compact thermal lithium atom beam source for measurements of electron velocity distribution function anisotropy in electron cyclotron resonance plasmas.
Author(s)	Nishioka, T; Shikama, T; Nagamizo, S; Fujii, K; Zushi, H; Uchida, M; Iwamae, A; Tanaka, H; Maekawa, T; Hasuo, M
Citation	The Review of scientific instruments (2013), 84(7)
Issue Date	2013-07-23
URL	http://hdl.handle.net/2433/179484
Right	© 2013 AIP Publishing LLC
Type	Journal Article
Textversion	publisher

Development of a compact thermal lithium atom beam source for measurements of electron velocity distribution function anisotropy in electron cyclotron resonance plasmas

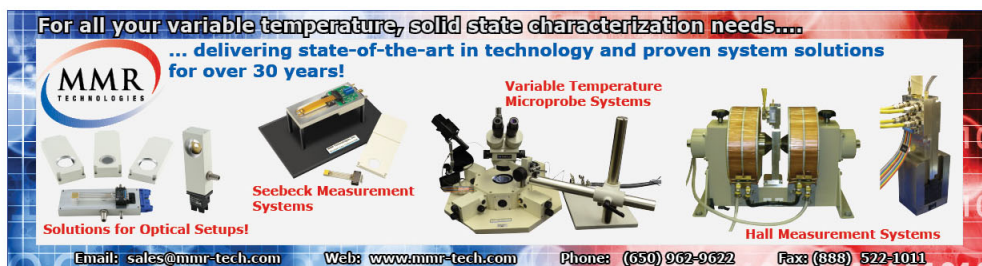
T. Nishioka, T. Shikama, S. Nagamizo, K. Fujii, H. Zushi, M. Uchida, A. Iwamae, H. Tanaka, T. Maekawa, and M. Hasuo

Citation: [Review of Scientific Instruments](#) **84**, 073509 (2013); doi: 10.1063/1.4815721

View online: <http://dx.doi.org/10.1063/1.4815721>

View Table of Contents: <http://scitation.aip.org/content/aip/journal/rsi/84/7?ver=pdfcov>

Published by the [AIP Publishing](#)



For all your variable temperature, solid state characterization needs....
... delivering state-of-the-art in technology and proven system solutions for over 30 years!

MMR TECHNOLOGIES

Seebeck Measurement Systems

Variable Temperature Microprobe Systems

Hall Measurement Systems

Solutions for Optical Setups!

Email: sales@mmr-tech.com Web: www.mmr-tech.com Phone: (650) 962-9622 Fax: (888) 522-1011

Development of a compact thermal lithium atom beam source for measurements of electron velocity distribution function anisotropy in electron cyclotron resonance plasmas

T. Nishioka,^{1,a)} T. Shikama,^{1,b)} S. Nagamizo,¹ K. Fujii,¹ H. Zushi,² M. Uchida,³ A. Iwamae,⁴ H. Tanaka,³ T. Maekawa,³ and M. Hasuo¹

¹*Department of Mechanical Engineering and Science, Graduate School of Engineering, Kyoto University, Kyoto 615-8540, Japan*

²*Research Institute for Applied Mechanics, Kyushu University, Fukuoka 816-8580, Japan*

³*Department of Fundamental Energy Science, Graduate School of Energy Science, Kyoto University, Kyoto 606-8502, Japan*

⁴*Research Center for Development of Far-Infrared Region, Fukui University, Fukui 910-8507, Japan*

(Received 1 April 2013; accepted 29 June 2013; published online 23 July 2013)

The anisotropy of the electron velocity distribution function (EVDF) in plasmas can be deduced from the polarization of emissions induced by anisotropic electron-impact excitation. In this paper, we develop a compact thermal lithium atom beam source for spatially resolved measurements of the EVDF anisotropy in electron cyclotron resonance (ECR) plasmas. The beam system is designed such that the ejected beam has a slab shape, and the beam direction is variable. The divergence and flux of the beam are evaluated by experiments and calculations. The developed beam system is installed in an ECR plasma device with a cusp magnetic field, and the LiI $2s-2p$ emission (670.8 nm) is observed in low-pressure helium plasma. The two-dimensional distributions of the degree and direction of the polarization in the LiI emission are measured by a polarization imaging system. The evaluated polarization distribution suggests the spatial variation of the EVDF anisotropy. © 2013 AIP Publishing LLC. [<http://dx.doi.org/10.1063/1.4815721>]

I. INTRODUCTION

New generation tokamaks equipped with superconducting magnetic field coils are limited in the maximum toroidal loop voltage induced by the changing magnetic flux. In order to reduce the voltage required for plasma initiation, ignition and current ramp-up scenarios assisted by electron cyclotron resonance (ECR) heating have been investigated.¹⁻⁵ Moreover, a fully non-inductive plasma initiation has been achieved in low-aspect ratio tokamaks.⁶⁻⁸ This technique could be utilized to remove the center solenoid coils of tokamaks and realize compact fusion reactors. In these plasma startup operations, the pre-ionized plasma is initially produced in the ECR layer. Electrons confined in a specific region of velocity space then spontaneously generate the initial plasma current. In conventional tokamaks, the following superposition of the ohmic electric field ramps up the current. Meanwhile, in low-aspect ratio tokamaks, the current is spontaneously developed by formation of the closed magnetic flux surface and the improvement of the electron confinement. In both the devices, the details of the mechanism by which the current develops are still not fully understood. An investigation of the temporal and spatial evolution of the electron velocity distribution function (EVDF), in particular, as for the production and relaxation of anisotropy in the EVDF as a measure of the electron confinement and current-drive, is

thus important to understand the detailed mechanisms of the plasma startup process and how to optimize it.

The diagnostic techniques of EVDF anisotropy—especially applicable in low temperature and density plasmas like those of the startup phase of tokamaks—have been investigated, e.g., electrical probes,^{9,10} a directional energy analyzer,¹¹ Thomson scattering,^{12,13} absorption of waves,¹⁴⁻¹⁶ and polarization in emission of atoms and ions.¹⁷ Among these techniques, the spectroscopy of polarized emission is non-perturbative and can be easily utilized under various plasma parameters by appropriately selecting the emission lines. It is well known from electron beam impact experiments and theoretical calculations that non-uniform population distributions of excited magnetic substates, namely, alignment, are created by anisotropic electron-impact excitation,¹⁸ and the subsequent emission is polarized. The degree and direction of the polarization depend on the magnitude and direction of the incident electron velocity. Anisotropy in the EVDF thus can be deduced in principle from the observed degree and direction of polarized emission.¹⁹⁻²¹ In the actual observation of plasmas, however, some issues should be considered. First, the observed polarization becomes an intensity-weighted average along the viewing chord. Second, population in excited states is produced not only by electron-impact excitation from the electronic ground state, but also by other processes: electron-impact and radiative de-excitations from upper states and radiation re-absorption. In order to take into account all the populating processes as functions of the electron density and anisotropic EVDF, collisional-radiative analysis which includes the transitions among magnetic substates is generally required. The model is called population-alignment colli-

^{a)}Current address: The Chugoku Electric Power Co., Inc., Shimane 690-0393, Japan.

^{b)}Author to whom correspondence should be addressed. Electronic mail: shikama@me.kyoto-u.ac.jp.

sional radiative (PACR) model.^{21,22} Unfortunately, although the theoretical framework of the PACR model includes a generalized treatment of the EVDF anisotropy, calculation results made so far appear to have limitations in accuracy that might originate from lack of the excitation cross-section data resolved into magnetic substates, as well as limitations in the precision of the available data.

For application of the polarization spectroscopy technique to plasmas without suffering these drawbacks, we have developed a compact thermal lithium atom beam source and observed the polarization of the lithium atom (LiI) $2s-2p$ emission (670.8 nm) from the injected beam. The lithium beam probe technique has been widely applied to tokamaks and stellarators²³⁻³³ for spatial profile measurements of the electron density and its fluctuation. Since lithium is a low- Z element and the beam probe technique uses a small number of particles compared to the background plasma density, the effect of the beam injection on plasmas is relatively small. The above-mentioned first drawback of the conventional technique, the spatial resolution, can be resolved by observing localized emission from the injected beam. For the second drawback, the limitation of available cross-section data resolved into magnetic substates, the population flowing into the lithium $2p$ state is dominated by electron-impact excitation from the ground state, regardless of the electron temperature and density. We therefore only need the cross-section data for electron-impact excitation from the $2s$ to $2p$ states. For this excitation process, reliable cross-section data evaluated by beam-impact experiments and theoretical calculations is available, so that we can reduce uncertainty in the determination of the electron energy from the observed degree of polarization. In order to confirm the feasibility of the diagnostic technique, we installed the developed beam source in an ECR plasma device with a cusp magnetic field and measured the two-dimensional spatial distributions of the degree and direction of polarization in the LiI $2s-2p$ emission.

II. POLARIZATION OF LiI $2s-2p$ EMISSION BY ELECTRON IMPACT

The polarization of the LiI $2s-2p$ emission by anisotropic electron-impact excitation has been evaluated both by experiments^{34,35} and calculations.³⁶⁻⁴¹ The degree of polarization is expressed as

$$P_0 = \frac{I_{\parallel} - I_{\perp}}{I_{\parallel} + I_{\perp}}, \quad (1)$$

where I_{\parallel} and I_{\perp} are the intensities of emission linearly polarized parallel and perpendicular to the electron beam, respectively, when emission is observed at right angles to the beam. The positive and negative signs of P_0 represent the direction of polarization, parallel and perpendicular to the quantization axis defined by the beam, respectively. The values of P_0 for ${}^6\text{Li}$, ${}^7\text{Li}$, and lithium with a natural isotopic composition (7.5% ${}^6\text{Li}$ + 92.5% ${}^7\text{Li}$) in terms of the incident electron energy³⁵ are shown in Fig. 1. Errors in the data are reported to be less than about 10%. In the presence of an external magnetic field, the quantization axis is defined by the field direction. The Larmor motion of the incident electron azimuthally

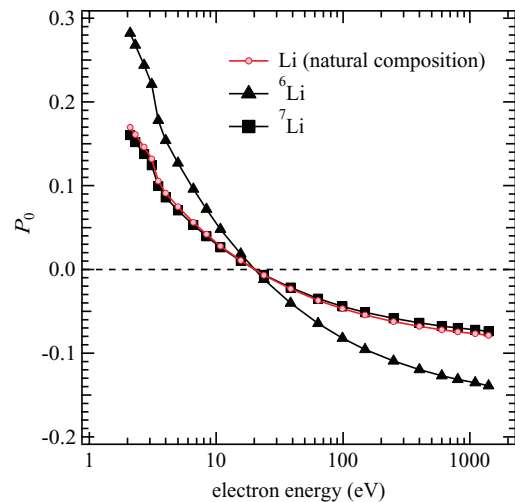


FIG. 1. The evaluated degree of polarization P_0 for the LiI $2s-2p$ emission by electron beam impact experiments.³⁵ The open circles denote lithium with a natural isotopic composition (7.5% ${}^6\text{Li}$ + 92.5% ${}^7\text{Li}$), crosses denote ${}^6\text{Li}$, and pluses denote ${}^7\text{Li}$.

averages polarization with respect to the field direction. The degree of polarization is then written¹⁹ as

$$P(\alpha, \beta) = \frac{P_0 \sin^2 \beta (3 \cos^2 \alpha - 1)}{2 - P_0 (2 \cos^2 \alpha \cos^2 \beta + \sin^2 \alpha \sin^2 \beta)}, \quad (2)$$

where α is the electron velocity pitch angle with respect to the magnetic field, and β is the angle between the direction of the emitted photon toward the observer and the field. The positive and negative signs of $P(\alpha, \beta)$ have the same meaning as before. If the electrons have a velocity distribution, the numerator and denominator of Eq. (2) should be integrated over the EVDF.^{19,20} Thus, it is not easy to make a quantitative evaluation of the EVDF from only the observed polarization. However, if we assume that the anisotropic electrons have a single energy, the energy of the electrons and the directional tendency of their velocity vectors, close to parallel/perpendicular to the magnetic field, can be deduced, and a comparison with the theoretical or numerical predictions of the electron dynamics in the tokamak plasma initiation process is possible.

The data in Fig. 1 are based on electron beam experiments. The condition corresponds to a low electron density plasma. The polarization degree could differ in plasmas with higher electron densities because of changes in the populating process of the upper excited state. In order to confirm the populating processes in terms of the electron density and temperature, we carried out collisional-radiative (CR) analysis of lithium atoms under an assumption of isotropic and thermalized EVDF. Details of the model are summarized in the Appendix. Fig. 2 shows the calculated fractions of the ionizing component flowing into the $2p$ state when $T_e = 10$ eV, where T_e is the electron temperature. In the figure, the area denoted as $2s$ indicates the fraction originating from electron-impact excitation from the $2s$ state, whereas the other areas indicate fractions by electron-impact and radiative de-excitations from upper excited states. We can see that the direct excitation is dominant—about 85%–90%—and the variation of the fraction with n_e is small unless n_e exceeds 10^{19} m^{-3} , where n_e is the

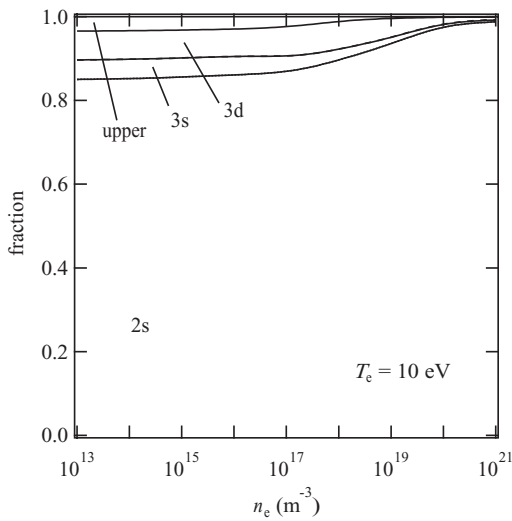


FIG. 2. The fraction of the population flux flowing into the $2p$ state as a function of n_e when $T_e = 10$ eV. The areas denoted as $2s$, $3s$, and $3d$ indicate the fractions originating from the designated electronic states, and that denoted as upper indicates the fraction from the other upper states.

electron density. If we fix n_e and change T_e instead, then the direct excitation fraction decreases with increasing T_e , and nearly reaches a constant value above 5 eV. The data in Fig. 1 thus can be extended without significant errors to plasmas with larger electron densities.

Since $\text{LiI } 2s-2p$ is a resonant transition, the reabsorption of emission could affect the polarization.⁴² The absorption coefficient at the peak of the spectral line profile, which is a measure of the reabsorption, is of the order of 10^{-8} m^{-1} in the present measurements. We use a slab beam with a thickness of about 20–30 mm, and observe the emission nearly normal to the plane of the beam. The effect of the reabsorption is thus negligibly small.

III. DEVELOPMENT OF A COMPACT THERMAL LITHIUM ATOM BEAM SOURCE

A. A compact thermal lithium atom beam source

We have designed and constructed a thermal lithium atom beam source. The design of the components is based on a previously developed beam source.³³ The main features distinguishing the present source from the previous one is a downsizing from a conflat 152 to a 114 flange for installation in small laboratory plasma devices, and the variability of the beam direction for flexible spatial measurements. Fig. 3 shows schematic cross-section drawings of the beam source, which consists of a vacuum chamber, oven, shutter, and three apertures. All the components are made of stainless steel. Lithium vapor is produced from solid lithium heated in the oven surrounded by a stainless sheath heater (Sukegawa Electric Co.; 300 W). The vapor is ejected through seven nozzles, each of which has a diameter of 2 mm and length of 15 mm. The outer surface temperature of the oven in the proximity of the nozzles is monitored by a K-type thermocouple (Hakko Electric Co. HTK1906) connected to a data acquisition module (National Instruments NI9211). We assume that the measured temperature reflects that of the vapor. After passing through the three apertures, the vapor is reduced to a slab beam with the thermal velocity distribution. The last aperture, which is separated by 67 mm from the exit of the nozzles, has a rectangular hole with dimensions of 2.0×20 mm in the x - and z -directions, respectively, where the x - and z -directions are defined in Fig. 3. The aperture is movable in the x -direction by a linear screw drive. The relative x -position of the aperture with respect to the nozzles determines the direction and divergence of the beam. The distance from the exit of the nozzles to the end of the vacuum chamber is 133 mm. During operation, the chamber is evacuated by a turbo molecular pump, and the pressure is monitored by an ionization gauge.

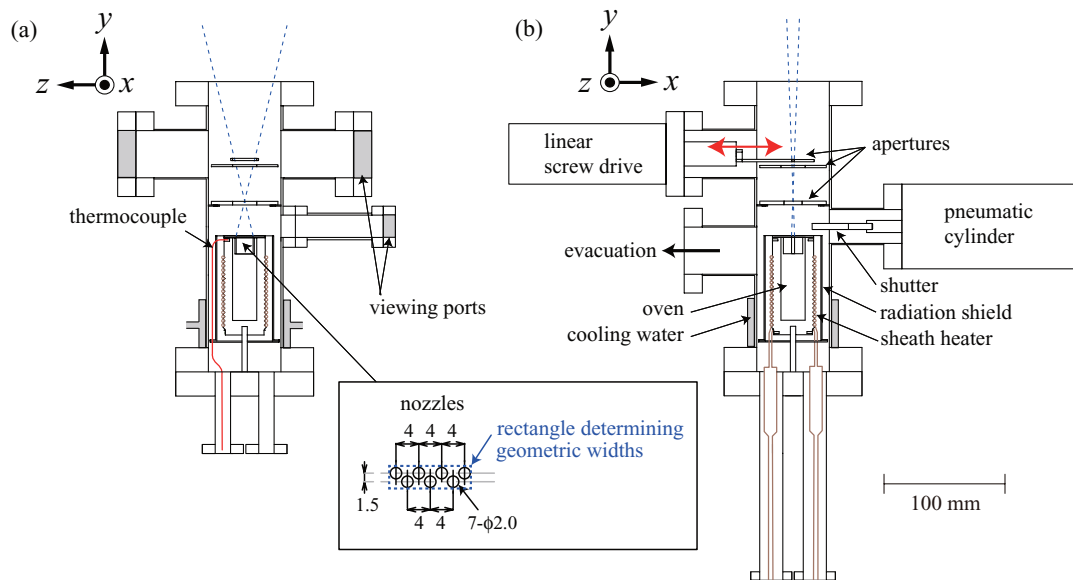


FIG. 3. The schematic cross-section drawings of the compact thermal lithium atom beam source: (a) front view, (b) side view. The $\{xyz\}$ coordinate system is defined as shown in the figure. The origin of the coordinate system is at the center of the nozzle surface.

The outer surface of the vacuum chamber is cooled by water at 20 °C.

B. Beam divergence

The lithium beam ejected from the oven nozzles undergoes collisions with electrons, ions, and neutrals in the plasmas. Collisions with ions and neutrals can change the trajectories of the lithium atoms, and this increases the divergence of the beam. In these experiments, the ion density ($< \sim 1 \times 10^{17} \text{ m}^{-3}$) is nearly an order smaller than the neutral density ($6 \times 10^{17} \text{ m}^{-3}$). We therefore neglect the collisions with ions and only take into account the collisions with neutrals. We evaluated the divergence based on a random walk simulation. In the simulation, the orthogonal $\{xyz\}$ coordinate system is defined as shown in Fig. 3; the origin of the system is at the center of the nozzle surface. We define the z -axis as parallel to the symmetric axis of the experimental device (see Fig. 6). The center of the last aperture is located at $x = 5 \text{ mm}$ in accordance with the experimental setup. The simulation was carried out with the following procedure.

- (1) An initial lithium atom is generated at $y = 0$. The (x, z) -coordinate position of the atom is determined randomly such that the position is within the circular areas of the seven nozzles. The velocity of the atom is determined probabilistically based on a Maxwell-Boltzmann distribution with a temperature of 843 K, the temperature adopted in the experiments. The most probable velocity is 1.4 km/s. The direction of the velocity is assumed to be isotropic and randomly selected.
- (2) The atom is forwarded along the velocity vector with a time step of 100 ns. In every step, the probability of the elastic collision with background neutrals is calculated. The cross-section of the collision is approximated as

$$\sigma = \pi(a_{\text{Li}} + a_{\text{gas}})^2, \quad (3)$$

where a_{Li} and a_{gas} are the atomic radii of lithium and background neutrals, respectively. The temperature of the background neutrals is assumed to be 300 K, and their velocity vectors are determined in the same way as described in step (1). The rate coefficient is then calculated using the relative velocity. The collision is detected by comparing a random number with the probability of the collision. If collision occurs, the scattering angle of the lithium atom in the center-of-mass frame is determined randomly. This assumption is an overestimation of the differential cross-section for large angle scattering compared to, for instance, the differential cross-section of Rutherford scattering.

- (3) Step (3) is repeated until the atom reaches the designated y -position. The (x, z) coordinate position of the atom is then recorded. The calculation is terminated if the atom impinges on the chamber wall or apertures.

The above procedure was repeated for 10^5 atoms. We used helium with a pressure of 2.5 mPa as a background gas. Fig. 4 shows the recorded (x, z) -coordinate positions at $y = 340 \text{ mm}$, corresponding to nearly the center of the view in the experiments. Histograms of the number of the atoms in the

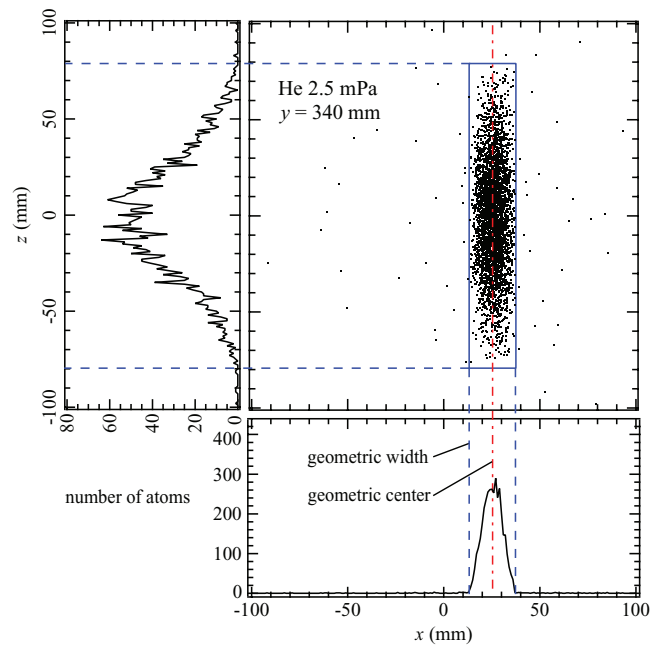


FIG. 4. The recorded (x, z) -coordinate positions of lithium atoms at $y = 340 \text{ mm}$ in 2.5 mPa helium gas atmosphere. The left and bottom figures show histograms of the number of the atoms in the z - and x -directions, respectively. The geometric widths are indicated by the lines. The geometric center in the x -direction is indicated by the vertical dashed line.

x - and z -directions are plotted together. If the beam undergoes no collision, then the maximum divergence is determined by the lines linking the edges of a rectangle that encompasses the seven circular nozzles (see inset in Fig. 3) and the edges of the last aperture. We denote the beam width in this case as “geometric width.” The geometric widths are indicated by the lines in Fig. 4. The geometric center of the beam in the x -direction, which is determined by the line linking the center line of the rectangle encompassing the nozzles and that of the last aperture, is indicated by the vertical dashed-dotted line. It can be seen that, under these experimental conditions, most atoms travel within the geometric widths. Note that although collision between lithium atoms was neglected in this simulation, it could be significant in the vicinity of the nozzles, where the lithium atom density is relatively large. This effect was, however, found to be relatively small in a preceding study,³³ in which the beam width ejected from a similar beam source was measured to be close to the geometric one. The spatial resolution of the measurements can thus be evaluated using the geometric width of the beam in the x -direction.

C. Beam flux

The oven temperature dependence of the lithium beam flux was measured by using a quartz microbalance (QMB) (an INFICON front load single sensor 983-9074 and IC/5 thin film deposition controller). The flux was evaluated from the deposition rate of lithium film.⁴³ The centers of the last aperture and the QMB were set to $x = 0 \text{ mm}$, and the QMB was located at $y = 173.5 \text{ mm}$ with its face normal to the y -direction. The diameter of the QMB sensor is 14 mm, while the geometric width of the beam in the x - and z -directions at the sensor

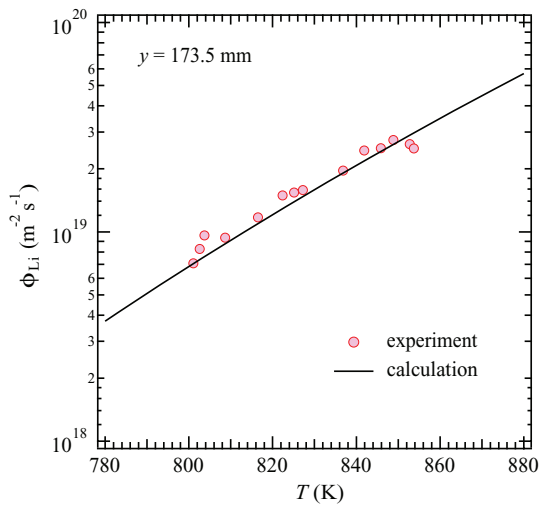


FIG. 5. The oven temperature dependence of the lithium atom flux at $y = 173.5$ mm. The circles represent the experimental data, while the line represents the calculation.

are 11 and 85 mm, respectively. In the calculation of the flux, we assumed for simplicity a uniform lithium density distribution over the effective area of the QMB sensor. The flux was recorded while raising the oven temperature up to 860 K. The measured fluxes are plotted with circles in Fig. 5. The measurements were compared with a theoretical curve. We assume that the ejected flux ϕ_{Li} can be expressed as

$$\phi_{\text{Li}} = C \Delta p, \quad (4)$$

where C is a constant, and Δp is the difference between the pressures inside and outside the oven. Δp was evaluated from the measured pressure outside and saturated vapor pressure inside calculated using the Antoine equation⁴⁴

$$\log_{10} p = 9.98831 - \frac{7918.984}{T - 9.52}, \quad (5)$$

where p is the vapor pressure. The calculated flux was least-squares fitted to the experimental data with varying C in Eq. (4). In Fig. 5, the fitting result is shown with a line. The temperature dependence is well represented by the calculation between 800 and 850 K.

IV. EXPERIMENTS

A. Polarization imaging system

The polarization state of light can be uniquely determined by measuring the Stokes parameters: I , Q , U , and V . We assume here that a non-uniform population distribution in the magnetic substates with $\pm M$, where M is the magnetic quantum number, namely, orientation, is not produced. In this case, V becomes zero. The observed emission can then only have linear polarization. The degree of polarization P and its azimuthal angle ϕ can be obtained from the Stokes parameters as

$$P = \frac{\sqrt{Q^2 + U^2}}{I}, \quad (6)$$

and

$$\phi = \frac{1}{2} \arctan \left(\frac{U}{Q} \right). \quad (7)$$

A polarization imaging system was used to obtain two-dimensional distributions of I , Q , and U . The system consists of a cooled CCD (FLI ML1109; 2048×506 pixels, $12 \mu\text{m}$ -square pixel, cooled down to -20°C) connected sequentially with a varifocal camera lens (Nikon Zoom-NIKKOR; focal length 35–70 mm), rotatable linear polarizer (Edmund Optics NT36-441), and a narrow-band interference filter (CVI Melles Griot F03-670.8-4-50.0M; peak wavelength 670.8 nm, FWHM 3 nm). The focal length and F-number of the lens were fixed to 57 mm and F/3.3, respectively. The extinction ratio of the polarizer was measured to be 1.9×10^{-3} . Note that the oblique incidence of light to the interference filter results in the shift of the transmission peak toward a shorter wavelength. Since the angle from the normal of the interference filter to the line connecting each CCD pixel and center of the diaphragm in the camera lens varies with the position on the CCD, the peak transmission wavelength also changes. The wavelength shift of the adopted filter, however, does not have s - and p -polarization dependence. The effect of the filter on polarization measurements thus can be neglected.

The relative sensitivities of the imaging system to linearly polarized light in 0° , 45° , 90° , and 135° directions were calibrated. Unpolarized continuum light was produced by reflecting light from a halogen lamp on a diffuse reflectance plate (Labsphere SRT-99-050). The reflectance plate was located 530 mm from the CCD chip. The position corresponds to the mid-plane of the vacuum chamber in the actual experiments (see Fig. 6). In order to take into account the effect of reflection on the viewing port, an identical quartz window whose normal was inclined by 14° to the optical axis, the same angle as the actual measurements, was inserted at the corresponding position. The distance from the CCD chip to the center of the window was 170 mm. The images of the reflectance plate were then taken by setting the transmission axis of the linear polarizer randomly in 0° , 45° , 90° , and 135° directions. After subtracting the background images taken without turning on the lamp, the relative sensitivities of each CCD pixel were evaluated. The variation of the relative CCD counts within the region used for measurements is less than about 5%.

B. ECR plasma device with a cusp magnetic field

Experiments were carried out in an ECR plasma device with a cusp magnetic field.^{21,45} Schematic cross-sectional drawings of the apparatus are shown in Fig. 6. The vacuum chamber consists of a rectangular part, with inner dimensions of $480 \text{ mm} \times 480 \text{ mm} \times 100 \text{ mm}$, and two cylindrical parts, with inner diameters of 256 mm and lengths of 170 mm, protruding from the rectangular part. The cylindrical parts are surrounded by three pairs of magnetic field coils. An internal conductor to create an additional azimuthal magnetic field is installed along the axis of the cylinders, but was not used. The device was evacuated by a turbo molecular pump, and the base pressure measured by an ionization gauge is lower than

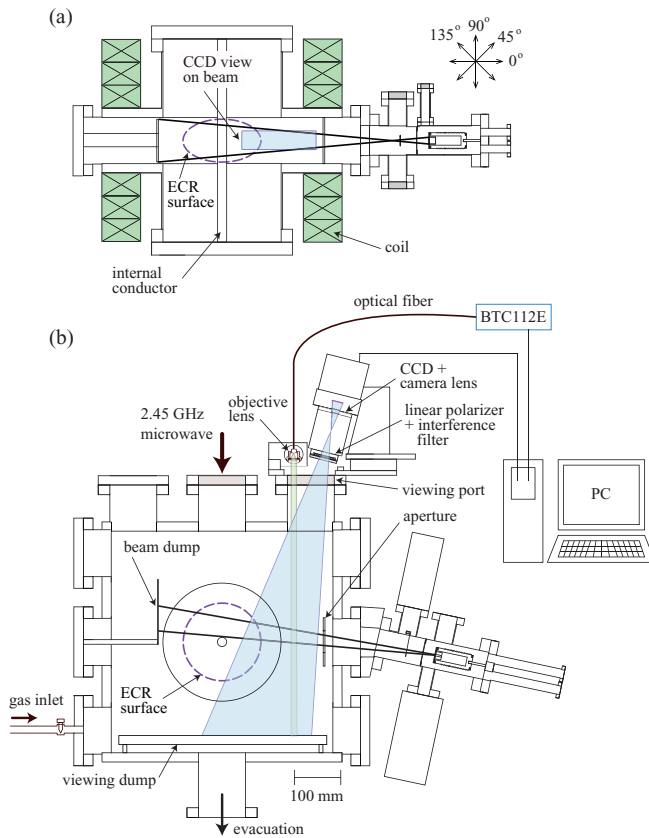


FIG. 6. The schematic cross-section drawings of the ECR plasma device with a cusp magnetic field: (a) yz -plane view, (b) xy -plane view. The angles used for the polarization measurements are illustrated in (a).

0.1 mPa. During operation, helium gas was continuously fed through a needle valve. By controlling the flow rate, the total pressure was adjusted to 1.7 mPa. At the onset of discharge, a 1 kA current with a duration of about 6 s was applied to the coils. Microwaves with a frequency of 2.45 GHz and a power of 830 W were then injected for 5 s through a quartz window from the top of the vacuum chamber. Plasma is initiated on the ECR surface, where the magnetic field strength is 87.5 mT. The ECR surface is a spheroid with major and minor axes of 168 mm and 92 mm, respectively.

The developed lithium beam source is horizontally attached to the rectangular part of the plasma device through a tapered reducer. The y -direction of the beam chamber is inclined by 12° upward to the horizontal direction. An additional aperture to prevent the beam from contacting the cham-

ber wall is installed, and this aperture slightly reduces the width of the beam in the z -direction. At the opposite side of the chamber, a beam dump made of stainless steel is installed. The beam was operated at a temperature of about 843 K. During operation, the total pressure increased slightly to 2.5 mPa presumably due to the desorption of impurities from the surface of lithium. We set the center of the last aperture to $x = 5$ mm and injected the beam in a direction 8° upward from the horizontal direction, as shown in Fig. 6.

The emission was observed from the top of the chamber using the polarization imaging system. The optical axis of the system was inclined by 14° to the vertical direction. The view corresponds to $r = 57\text{--}207$ mm and $z = -20.5$ to 17.5 mm, where r is the radius from the axis of the cylindrical chambers. The far side of the view was partially blocked by the neck of the port. The asymmetry in the range of z is due to a slight misalignment of the imaging system. The spatial resolution of the measurements determined by the geometric width of the beam in the x -direction is 20–33 mm, changing from the near to far side of the view. On the bottom of the rectangular chamber, a viewing dump made of stacked black-colored aluminum plates of various heights is installed to reduce reflection.

The transmission axis of the linear polarizer was randomly set to one of the 0° , 45° , 90° , and 135° directions in every discharge, and polarization images were measured at times when the discharge reached a steady state. The directions of the transmission axis are schematically illustrated by the double-headed arrows in Fig. 6. The images measured without injecting microwaves were used as backgrounds. Additionally, emission spectra in a wavelength range 200–900 nm were measured by a spectrometer (B&W Tek BTC112E) with a wavelength resolution of 1.2 nm (FWHM) at 546 nm. The viewing chord has a diameter of 11 mm and was directed vertically downward from the top of the chamber. The intensities of measured spectra were calibrated using a standard lamp.

V. RESULTS

A measured polarization image with the transmission axis of the linear polarizer in the 0° direction is shown in Fig. 7. A fan-shaped emission along the cusp magnetic field lines is observed. In the figure, the ECR surface is indicated by the dashed line, and the intersection of the spectrometer viewing chord and the lithium beam is indicated by the open circle.

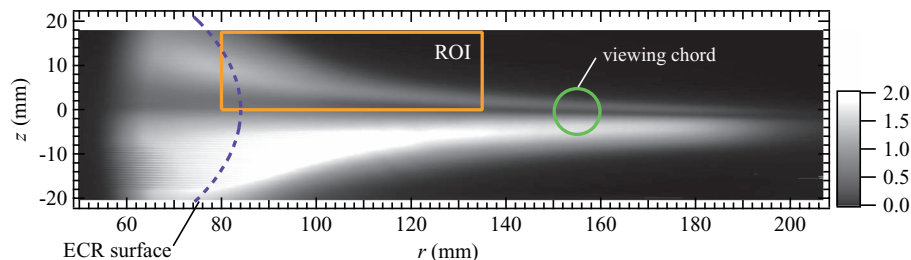


FIG. 7. A polarization image of the helium plasma with injecting the lithium beam and setting the transmission axis of the linear polarizer in the 0° direction. The color represents the intensity in arbitrary units (not calibrated). The ECR surface is designated by the dashed line, and intersection of the spectrometer viewing chord and the lithium beam is indicated by the open circle. The rectangular region surrounded by the line is the region of interest used for analysis.

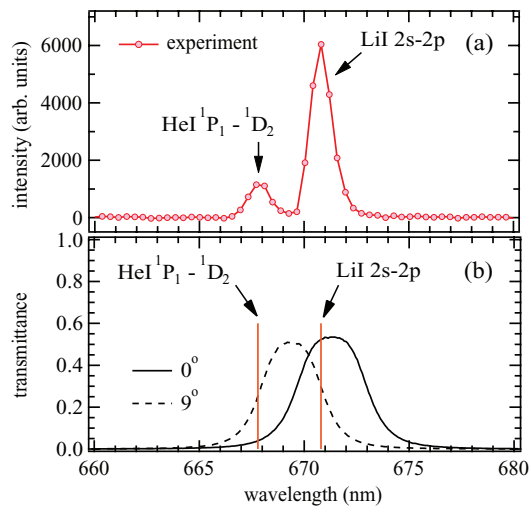


FIG. 8. (a) The LiI $2s-2p$ and HeI $^1P_1-^1D_2$ spectral lines measured by the spectrometer. (b) Transmittance curves of the interference filter with incidence angles of 0° and 9° . The wavelengths of the LiI and HeI transitions are indicated by the vertical lines.

The color of the image represents the emission intensity in arbitrary units. Although the relative sensitivities among the CCD pixels are not calibrated, the emission intensity tends to decrease toward the symmetric plane of the cusp magnetic field ($z = 0$) as well as toward the plasma edge (see also Fig. 9(a)). The observed asymmetry of the intensity between the upper- and lower-half regions is because of perturbation by a Langmuir probe inserted in the lower-half region.⁴⁵

The LiI $2s-2p$ spectrum measured by the spectrometer, is shown in Fig. 8(a). Since the wavelength resolution of our imaging system is 3 nm, the HeI $^1P_1-^1D_2$ (667.8 nm) emission is mixed into the LiI $2s-2p$ emission. Fig. 8(b) shows the transmittance curves of the interference filter with incidence angles of 0° and 9° measured using a halogen lamp and another spectrometer (JASCO CT100-CP; focal length 1.0 m, 300 grooves/mm grating) coupled with a cooled CCD (Roper Scientific 1100PB; 1100×300 pixels, $24 \mu\text{m}$ -square pixel, cooled down to -196°C). The incidence angles of 0° and 9° correspond to the center and edge regions of the CCD; the latter is around $r = 60$ and 190 mm in Fig. 7. The angles are evaluated from the normal of the interference filter to the line connecting the CCD pixel and center of the diaphragm in the camera lens. In order to resolve the LiI image, the HeI image measured in a discharge without injecting the lithium beam was subtracted under an assumption that the spatial profile of the HeI emission does not change while injecting the beam. The subtraction was carried out as follows:

- (1) Polarization images taken with and without injection of the lithium beam are measured with exposure times of 0.3 and 1.5 s, respectively. The background images are subtracted from them, and the images are normalized to each exposure time. These images are denoted $I_{\text{He} + \text{Li}}$ and I_{He} , respectively.
- (2) Spectra are measured by the spectrometer with exposure times of 0.1 and 1.0 s. The background spectra are subtracted from them, and the intensities are normalized to each exposure time. The spectra are then least-squares

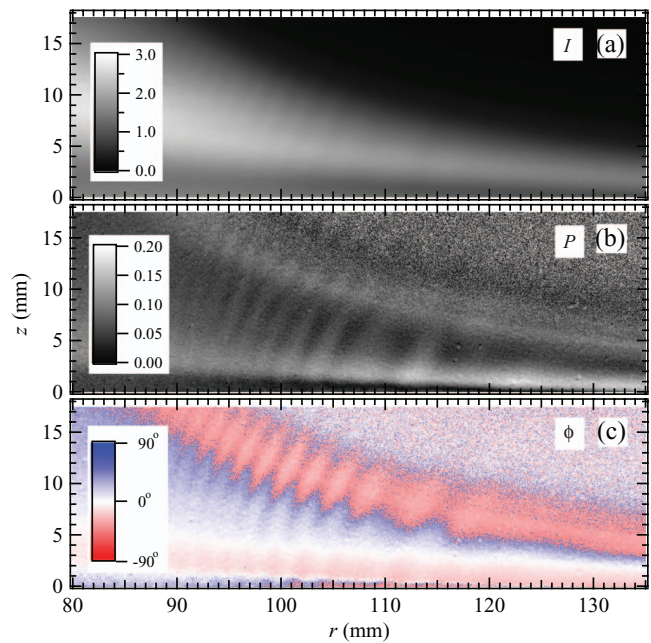


FIG. 9. The images of (a) the Stokes parameter I in arbitrary units, (b) the degree of polarization P , and (c) the azimuthal angle of the linear polarization ϕ in degrees.

fitted by double and single Gaussian functions, respectively. The HeI spectral line intensities are evaluated as areas of the Gaussian function. The ratio between the HeI spectral line intensities with and without the beam injection is denoted by $R_{(\text{He} + \text{Li})/\text{He}}$.

- (3) The LiI image I_{Li} is obtained by subtracting $R_{(\text{He} + \text{Li})/\text{He}} I_{\text{He}}$ from $I_{\text{He} + \text{Li}}$. Since the lithium beam flux slightly fluctuates with time due to changes in the oven temperature, the variation of I_{Li} in successive discharges is compensated by normalizing I_{Li} to the LiI spectral line intensity measured by the spectrometer.

In the above procedure, the evaluated values of $R_{(\text{He} + \text{Li})/\text{He}}$ are larger than about 0.9. It is thus confirmed that perturbation caused by the beam injection is small. The variation of the LiI intensities is smaller than 10% for successive discharges. The upper-half of the image in Fig. 7 was used for analysis to avoid perturbation by the Langmuir probe. In the figure, the region of interest used for analysis is highlighted by the rectangle. Fig. 9 shows the evaluated images of (a) the Stokes parameter I in arbitrary units, (b) the degree of polarization P , and (c) the azimuthal angle ϕ in degrees. In Fig. 9(b), P becomes larger in the plasma edge and symmetric plane regions of the cusp magnetic field, while it becomes smaller in the intermediate region. Note that P does not become zero even outside the plasma. This is likely due to a small amount of reflected light from the viewing dump. In Fig. 9(c), ϕ has opposite signs in the edge/symmetric plane and intermediate regions. The angle becomes nearly zero outside the plasma. In a portion of Fig. 9, interference patterns, which may originate from the curvature of the camera lens, are observed. The appearance of the pattern may be because of slight differences in the window positions between the calibration and experiment.

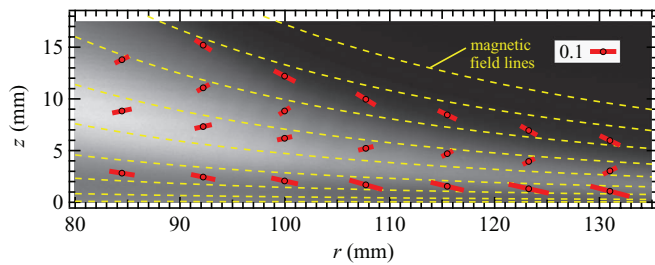


FIG. 10. The spatially averaged P and ϕ over 5×5 pixels (0.4 mm-square) at discrete positions. The length and direction of the bars represent the degree and direction of the polarization, respectively. The dashed lines show the magnetic field lines.

Figure 10 represents plot of P and ϕ at discrete positions on the image of I . In the figure, the magnetic field at the center of the beam is indicated by dashed lines. The length and direction of the bars represent the degree and direction of the polarization, respectively; the values are spatially averaged over 5×5 pixels corresponding approximately to 0.4 mm-square region. It can be seen that the polarization is directed nearly parallel to the field lines in the edge and symmetric plane regions. The degree of polarization is about 0.1–0.15. Meanwhile, in the intermediate region, the polarization is directed nearly perpendicular to those in the edge and symmetric plane regions and is rather close to perpendicular to the field lines. The degree is smaller, about 0.05. We denote the former and latter regions as regions (i) and (ii), respectively. Theoretically, the direction of polarization should be either parallel or perpendicular to the magnetic field lines because of the azimuthally symmetric Larmor motion of the electrons. Possible causes of the deviation from these directions are the effect of the emission integral over the beam thickness and that of the reflected light.

From Fig. 1, two interpretations are possible for the observed polarization. One is low energy electrons (≤ 20 eV) moving along the direction of polarization, and the other is high energy electrons (≥ 20 eV) moving in a direction perpendicular to the direction of polarization. If we approximate $\alpha = 0^\circ$ or 90° and $\beta = 90^\circ$ in Eq. (2), then the equation can be simplified as

$$P(\alpha = 0^\circ, \beta = 90^\circ) = P_0, \quad (8)$$

or

$$P(\alpha = 90^\circ, \beta = 90^\circ) = \frac{P_0}{P_0 - 2}. \quad (9)$$

If we assume that the averaged velocity vector of the anisotropic electrons is directed parallel to the magnetic field, we can deduce from Eq. (8) that the average electron energy is about 2–4 eV in region (i). On the other hand, if we assume that the averaged velocity vector is directed perpendicular to the magnetic field, then the observed degree of the polarization is too large compared to the possible values calculated from Eq. (9) and Fig. 1. It should be mentioned, however, that in our experimental apparatus, X-rays with energy up to 20 keV were previously detected in an argon discharge with similar pressure and microwave power.⁴⁵ The larger degree of polarization may be expected with further increases to the

electron energy in Fig. 1. In region (ii), the estimated average electron energies are around 100 and 3 eV with the former and latter assumptions, respectively.

Although it is necessary to use other diagnostic techniques or to model the electron dynamics to determine the actual situation from these possible interpretations, the obtained spatial variation of the degree and direction of the polarization indicates that spatial variation of the EVDF anisotropy was detected. In order to remove the remaining uncertainty from these interpretations, a comparison of the present results with measurements found using other techniques is currently underway. In addition, for temporally resolved measurements, a new optical system is being developed.

VI. SUMMARY

We have designed and constructed a compact thermal lithium atom beam source for investigations of the spatial and temporal evolution of the EVDF anisotropy in ECR plasmas. The divergence of the beam was evaluated by a random walk simulation. Under low-pressure conditions using helium gas at 2.5 mPa, the divergence was determined by the geometric widths. The oven temperature dependence of the ejected atomic flux was measured by a quartz microbalance. The measured flux is well represented by a theoretical curve. The developed beam source was installed in an ECR plasma device with a cusp magnetic field. Linear polarization images of the LiII $2s-2p$ emission in the 0° , 45° , 90° , and 135° directions were measured using a polarization imaging system. The two-dimensional distributions of the Stokes parameters I , Q , and U , and the degree and direction of polarization were evaluated from the acquired images. The obtained polarization distribution suggests spatial variation of the EVDF anisotropy.

ACKNOWLEDGMENTS

T. Nishioka and T. Shikama are grateful to Professor T. Morisaki at the National Institute for Fusion Science for discussion about the design of the lithium beam source. This work was supported in part by the Grant-in-Aid for Scientific Research (A) No. 21246139 and the Grant-in-Aid for Young Scientists (B) No. 24740367 from the Japan Society for the Promotion of Science, and by the collaborative research program of the Research Institute for Applied Mechanics in Kyushu University.

APPENDIX : COLLISIONAL-RADIATIVE MODEL FOR LITHIUM ATOMS

Some CR models have been constructed for lithium atoms.^{46,47} In this work, we have implemented our own model and calculation code for flexible application to our diagnostic technique. Here, we briefly describe the energy levels and data sets included in our code. Further detailed discussions about the reliability of the data can be found in the references quoted below. General descriptions about the CR model can be found in standard textbooks, e.g., Refs. 48 and 49.

In our model, the electronic excited states of lithium atoms with $n \leq 30$ are included, where n is the principal

quantum number. In particular, states with $n \leq 9$ are resolved into the directional quantum number l . The states with $l \geq 3$ are bundled together, and these states are denoted as $f+$. The energies of the $n \leq 9$ states are taken from the NIST Database⁵⁰ and the work of Bashkin and Staner.⁵¹ Those of the $f+$ states are calculated as statistically weighted average of the bundled substates. The energies of the $n \geq 10$ states are calculated based on the hydrogen-like approximation as

$$E_n = E_{\text{Li}} - \frac{R_\infty}{n^2}, \quad (\text{A1})$$

where E_n is the energy of the state with the principal quantum number n , E_{Li} is the ionization energy of lithium atoms, and R_∞ is the Rydberg constant. The shielding of the nuclear potential by the inner electrons becomes more effective for excited electrons in states with large n . The hydrogen-like approximation provides reasonably accurate energies for these states. For instance, the difference between the energy calculated by Eq. (A1) and that in the references is about 0.1 eV for the $n = 9$ state. This error is not significant for the present purpose.

The spontaneous emission coefficients for all the transitions between the states with $n \leq 5$ and some of the transitions between the states with $6 \leq n \leq 9$ are quoted from the NIST Database⁵⁰ and from Wiese *et al.*⁵² The coefficients for the other transitions are calculated using the oscillator strengths evaluated in previous works.^{53–55} For the transitions between the $n \geq 10$ and $n \leq 9$ states, only the lower states are resolved into l -substates. The calculated coefficients in terms of the principal quantum numbers are then distributed based on an assumption that all the transitions between the included l -substates have the same coefficient.

For the electron-impact ionization, the cross-section evaluated by experiments⁵⁶ is adopted for the ground state ($2s$). The cross-sections calculated by the convergent close-coupling method⁵⁷ are used for the $2p$, $3s$, $3p$, and $3d$ states. For states with $4 \leq n \leq 9$, Lotz's empirical formula^{58,59} is used. In order to estimate errors in the calculated cross-sections, we applied the formula to the $n = 3$ states. The differences between the calculated cross-sections and those quoted from Schweinzer *et al.*⁵⁷ are as large as $\sim 100\%$. For the $n \geq 10$ states, the semi-empirical formula used by Johnson^{60,61} with the hydrogen-like approximation is adopted. For the $f+$ states, the cross-sections for the f states are used.

The electron-impact excitation cross-sections calculated by the convergent close-coupling method⁵⁷ are adopted for transitions between the $n \leq 4$ states. For excitations from the $n \leq 4$ to the upper states, n^3 scaling is assumed. Witthoef *et al.*⁶² pointed out that the scaling provides data with reasonable accuracy for the upper states with $n \geq 7$. Johnson's formula^{60,61} was used for the other transitions. When applying Johnson's formula to the transitions including the $n \leq 9$ states, the cross-sections are distributed following the statistical weights of the lower l -substates. The electron-impact de-excitation cross-sections can be obtained using the Klein-Rossland (detailed balance) relation.

The radiative and dielectric recombination cross-sections are taken from Badnell *et al.*^{63,64} The data are evaluated based

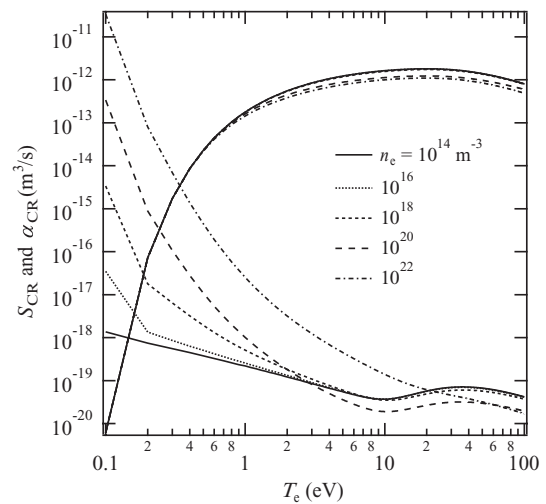


FIG. 11. The collisional-radiative ionization and recombination rate coefficients for lithium atoms as a function of T_e and n_e .

on calculations of the photo-ionization and auto-ionization cross-sections and the Klein-Rossland relation. The data provided in the references are only for discrete T_e values, so we interpolated the data by cubic-spline curve fitting. In addition, for the $n \geq 9$ states, only n -resolved data are provided for discrete values of n . The missing data are complemented by interpolation using cubic-spline curve fitting. For the $n = 9$ states, the cross-section is distributed for the l -substates by assuming that the cross-section is the same for all the substates. The three-body recombination cross-sections are evaluated from the ionization cross-sections by using the Klein-Rossland relation.

In the CR model, the rate equation for the ground state atoms can be expressed⁴⁹ as

$$\frac{dn_0}{dt} = -S_{\text{CR}}n_0n_e + \alpha_{\text{CR}}n_zn_e, \quad (\text{A2})$$

where n_0 is the population of the ground state atoms, n_e and n_z are the densities of electrons and singly ionized ions, respectively, and S_{CR} and α_{CR} are the so-called CR ionization and recombination rate coefficients, respectively. From the magnitude of these CR rate coefficients, we can determine if the populating process is dominated by excitation from the ground state atoms (ionizing) or recombination from the ions (recombining). Fig. 11 shows the calculated CR rate coefficients as functions of T_e and n_e . In our experimental conditions, in which we have approximately $T_e \geq 1$ eV and $n_e \leq 10^{17} \text{ m}^{-3}$, the lithium atoms are in the ionizing phase.

¹K. Kajiwara, Y. Ikeda, M. Seki, S. Moriyama, T. Oikawa, and T. Fujii, *Nucl. Fusion* **45**, 694 (2005).

²G. L. Jackson, J. S. deGrassie, C. P. Moeller, and R. Prater, *Nucl. Fusion* **47**, 257 (2007).

³J. Bucalossi, P. Hertout, M. Lennholm, F. Saint-Laurent, F. Bouquay, C. Darbos, E. Traisnel, and E. Trier, *Nucl. Fusion* **48**, 054005 (2008).

⁴Y. S. Bae, J. H. Jeong, S. I. Park, M. Joung, J. H. Kim, S. H. Hahn, S. W. Yoon, H. L. Yang, W. C. Kim, Y. K. Oh, A. C. England, W. Namkung, M. H. Cho, G. L. Jackson, J. S. Bak, and the KSTAR Team, *Nucl. Fusion* **49**, 022001 (2009).

⁵J. Stober, G. L. Jackson, E. Ascasibar, Y.-S. Bae, J. Bucalossi, A. Cappa, T. Casper, M.-H. Cho, Y. Gribov, G. Granucci, K. Hanada, J. Hobirck, A. W. Hyatt, S. Ide, J.-H. Jeong, M. Joung, T. Luce, T. Lunt, W. Namkung,

- S.-I. Park, P. A. Politzer, J. Schweinzer, A. C. C. Sips, the ASDEX Upgrade Team, the TJ-II Team, and the ITPA Integrated Operations Scenarios Group Members and Experts, *Nucl. Fusion* **51**, 083031 (2011).
- ⁶C. B. Forest, Y. S. Hwang, M. Ono, G. Greene, T. Jones, W. Choe, M. Schaffer, A. Hyatt, T. Osborne, R. I. Plnskerr, C. C. Petty, J. Lohr, and S. Lippmann, *Phys. Plasmas* **1**, 1568 (1994).
- ⁷T. Yoshinaga, M. Uchida, H. Tanaka, and T. Maekawa, *Phys. Rev. Lett.* **96**, 125005 (2006).
- ⁸M. Uchida, T. Yoshinaga, H. Tanaka, and T. Maekawa, *Phys. Rev. Lett.* **104**, 065001 (2010).
- ⁹H. Aikawa, *J. Phys. Soc. Jpn.* **40**, 1741 (1976).
- ¹⁰T. Shikama, S. Kado, S. Kajita, and S. Tanaka, *Jpn. J. Appl. Phys.* **43**, 809 (2004).
- ¹¹R. L. Stenzel, W. Gekelman, N. Wild, J. M. Urrutia, and D. Whelan, *Rev. Sci. Instrum.* **54**, 1302 (1983).
- ¹²M. D. Bowden, T. Okamoto, F. Kimura, H. Muta, K. Uchino, K. Muraoka, T. Sakoda, M. Maeda, Y. Manabe, M. Kitagawa, and T. Kimura, *J. Appl. Phys.* **73**, 2732 (1993).
- ¹³E. Yatsuka, T. Hatae, and Y. Kusama, *Nucl. Fusion* **51**, 123004 (2011).
- ¹⁴R. Kirkwood, I. H. Hutchinson, S. C. Luckhards, M. Porkolab, and J. P. Squire, *Phys. Fluids B* **2**, 1421 (1990).
- ¹⁵F. Skiff, D. A. Boyd, and J. A. Colbom, *Phys. Fluids B* **5**, 2445 (1993).
- ¹⁶D. J. Thuecks, F. Skiff, and C. A. Kletzing, *Rev. Sci. Instrum.* **83**, 083503 (2012).
- ¹⁷*Plasma Polarization Spectroscopy*, edited by T. Fujimoto and A. Iwamae (Springer, 2008).
- ¹⁸*Polarization, Alignment, and Orientation in Atomic Collisions*, edited by N. Andersen and K. Bartshat (Springer, 2000).
- ¹⁹E. Haug, *Sol. Phys.* **71**, 77 (1981).
- ²⁰J. C. Kieffer, J. P. Matte, H. Pépin, M. Chaker, Y. Beaudoin, T. W. Johnston, C. Y. Chien, S. Coe, G. Mourou, and J. Duau, *Phys. Rev. Lett.* **68**, 480 (1992).
- ²¹A. Iwamae, T. Sato, Y. Horimoto, K. Inoue, T. Fujimoto, M. Uchida, and T. Maekawa, *Plasma Phys. Controlled Fusion* **47**, L41 (2005).
- ²²T. Fujimoto and S. A. Kazantsev, *Plasma Phys. Controlled Fusion* **39**, 1267 (1997).
- ²³K. Kadota, K. Tsuchida, Y. Kawasumi, and J. Fujita, *Plasma Phys.* **20**, 1011 (1978).
- ²⁴A. Pospieszczyk and G. G. Ross, *Rev. Sci. Instrum.* **59**, 1491 (1988).
- ²⁵A. Pospieszczyk, F. Aumayr, H. L. Bay, E. Hintz, P. Leismann, Y. T. Lie, G. G. Ross, D. Rusbüldt, R. P. Schorn, B. Schweer, and H. Winter, *J. Nucl. Mater.* **162–164**, 574 (1989).
- ²⁶A. Komori, S. Nagai, T. Morisaki, and Y. Kawai, *Rev. Sci. Instrum.* **61**, 3787 (1990).
- ²⁷A. Komori, A. Yonesu, S. Nagai, T. Mizuuchi, M. Harada, H. Matsuura, F. Sano, H. Zushi, S. Sudo, M. Nakasuga, Y. Kawai, and T. Obiki, *Jpn. J. Appl. Phys.* **30**, 3526 (1991).
- ²⁸J. Schweinzer, E. Wolfrum, F. Aumayr, M. Pöckl, H. Winter, R. P. Schorn, and E. Hintz, *Plasma Phys. Controlled Fusion* **34**, 1173 (1992).
- ²⁹S. Sasaki, S. Takamura, M. Ueda, H. Iguchi, J. Fujita, and K. Kadota, *Rev. Sci. Instrum.* **64**, 1699 (1993).
- ³⁰S. Sasaki, S. Takamura, Y. Uesugi, Y. Ohkouchi, and K. Kadota, *Rev. Sci. Instrum.* **64**, 2277 (1993).
- ³¹A. Huber, U. Samm, B. Schweer, and Ph. Mertens, *Plasma Phys. Controlled Fusion* **47**, 409 (2005).
- ³²H. Tsuchiya, T. Morisaki, A. Komori, and O. Motojima, *Rev. Sci. Instrum.* **77**, 10F526 (2006).
- ³³H. Zushi, T. Morisaki, Y. Inada, J. Bouchard, K. Nakashima, H. Tsuchiya, K. Hanada, K. Sasaki, R. Bhattacharyay, K. N. Sato, K. Nakamura, M. Sakamoto, H. Idei, M. Hasegawa, S. Kawasaki, H. Nakashima, and A. Higashijima, *J. Nucl. Mater.* **363–365**, 1429 (2007).
- ³⁴H. Hafner and H. Kleinpoppen, *Z. Phys.* **198**, 315 (1967).
- ³⁵D. Leep and A. Gallagher, *Phys. Rev. A* **10**, 1082 (1974).
- ³⁶P. G. Burke and A. J. Taylor, *J. Phys. B* **2**, 869 (1969).
- ³⁷N. Feautrier, *J. Phys. B* **3**, L152 (1970).
- ³⁸P. McCavert and M. R. H. Rudge, *J. Phys. B* **3**, 1286 (1970).
- ³⁹E. Karule, *J. Phys. B* **3**, 860 (1970).
- ⁴⁰A. N. Tripathi, K. C. Mathur, and S. K. Joshi, *J. Phys. B* **6**, 1431 (1973).
- ⁴¹S. Kumar and M. K. Srivastava, *J. Phys. B* **9**, 1911 (1976).
- ⁴²M. Seo, M. Nimura, M. Hasuo, and T. Fujimoto, *J. Phys. B* **36**, 1869 (2003).
- ⁴³C.-S. Lu, *J. Vac. Sci. Technol.* **12**, 578 (1975).
- ⁴⁴NIST Chemistry Webbook (<http://webbook.nist.gov/chemistry/>).
- ⁴⁵M. Uchida, S. Fukumoto, M. Asakawa, H. Tanaka, T. Maekawa, and Y. Terumichi, *Jpn. J. Appl. Phys.* **38**, L885 (1999).
- ⁴⁶S. D. Loch, J. Colgan, M. C. Witthoef, M. S. Pindzola, C. P. Ballance, D. M. Mitnik, D. C. Griffin, M. G. O'Mullane, N. R. Badnell, and H. P. Summers, *At. Data Nucl. Data Tables* **92**, 813 (2006).
- ⁴⁷See <http://www.adas.ac.uk/> for ADAS codes.
- ⁴⁸H. R. Griem, *Principles of Plasma Spectroscopy* (Cambridge University Press, 1997), Chap. 6.
- ⁴⁹T. Fujimoto, *Plasma Spectroscopy* (Oxford University Press, 2004), Chap. 4.
- ⁵⁰NIST Atomic Spectra Database, version 4 (<http://www.nist.gov/pml/data/asd.cfm>).
- ⁵¹S. Bashkin and J. A. Staner, Jr., *Atomic Energy Levels & Grotrian Diagrams* (Elsevier, 1975).
- ⁵²W. L. Wiese, M. W. Smith, and B. M. Glennon, *Atomic Transition Probabilities. Volume I: Hydrogen Through Neon* (National Bureau of Standards, 1966).
- ⁵³W. J. Karzas and R. Latter, *Astrophys. J., Suppl.* **6**, 167 (1961).
- ⁵⁴L. C. Green, P. P. Rush, and C. D. Chandler, *Astrophys. J., Suppl.* **3**, 37 (1957).
- ⁵⁵D. H. Menzel and C. L. Pekeris, *Mon. Not. R. Astron. Soc.* **96**, 77 (1935).
- ⁵⁶D. Wutte, R. K. Janev, F. Aumayr, M. Schneider, J. Schweinzer, J. J. Smith, and H. P. Winter, *At. Data Nucl. Data Tables* **65**, 155 (1997).
- ⁵⁷J. Schweinzer, R. Brandenburg, I. Bray, P. Hoekstra, F. Aumayr, R. K. Janev, and H. P. Winter, *At. Data Nucl. Data Tables* **72**, 239 (1999).
- ⁵⁸W. Lotz, *Z. Phys.* **206**, 205 (1967).
- ⁵⁹W. Lotz, *Z. Phys.* **216**, 241 (1968).
- ⁶⁰L. C. Johnson, *Astrophys. J.* **174**, 227 (1972).
- ⁶¹R. K. Janev, D. Reiter, and U. Samm, "Collision processes in low-temperature hydrogen plasmas," Forschungszentrum Jülich Report No. Jül-4105, pp. 10–12.
- ⁶²M. Witthoef, J. Colgan, M. S. Pindzola, C. P. Balance, and D. C. Griffin, *Phys. Rev. A* **68**, 022711 (2003).
- ⁶³N. R. Badnell, *Astrophys. J., Suppl.* **167**, 334 (2006).
- ⁶⁴N. R. Badnell, M. G. O'Mullane, H. P. Summers, Z. Altun, M. A. Bautista, J. Colgan, T. W. Gorczyca, D. M. Mitnik, M. S. Pindzola, and O. Zatsarinny, *Astron. Astrophys.* **406**, 1151 (2003).